Characteristics of femtosecond laser-induced shockwaves in air

Olga Koritsoglou, Didier Loison, Olivier Uteza, Alexandros Mouskeftaras

Characteristics of femtosecond laser-induced shockwaves in air

OLGA KORITSOGLOU,[1,3] DIDIER LOISON,[2] OLIVIER UTEZA,[1] AND ALEXANDROS MOUSKEFTARAS[1,4,*] ⓘ

[1]*Aix Marseille Univ, CNRS, LP3 UMR 7341, Campus de Luminy, Case 917,13288, Marseille, France*
[2]*Institut de Physique de Rennes, CNRS, Université Rennes 1, F-35042 Rennes, France*
[3]*olga.koritsoglou@etu.univ-amu.fr*
[4]*alexandros.mouskeftaras@cnrs.fr*
[*]*alexandros.mouskeftaras@univ-amu.fr*

Abstract: Dynamic characteristics of femtosecond laser-generated shockwaves are investigated in ambient air. The experiments are performed using a 360-fs pulsed laser at a wavelength of 1.03 μm, with laser intensities up to 5×10^{14} W/cm^2 (corresponding to about five times the air breakdown intensity threshold). Plasma and shockwave generation and propagation are visualized using a time-resolved transmission microscope. The maximum propagation velocity is in the order of Mach 30. By implementing a simple theoretical model, we find an initial pressure loading in the GPa range and shockwave pressure dropping down to MPa following propagation over few micrometers away from focus.

1. Introduction

The unique features of femtosecond (fs) laser interaction with matter have enabled a wide, still expanding, range of applications [1,2]. This interaction has been the topic of intense research in the past decades [3–5] and although far from being fully understood, a general scenario is widely accepted. Following the fs laser-induced ionization, energy is deposited in a well localized volume. As a result, matter is brought to an extreme thermodynamic state with highly energetic electrons surrounding cold ions. In the direction of restoring the thermodynamic equilibrium, these electrons transfer their energy to their environment. Thus, an important gradient of pressure and temperature builds up inside the volume of the irradiated area, resulting in a violent decompression through emission of a shockwave (SW) which is a pressure wave propagating in the material with a speed faster than that of the local speed of sound. Fs laser-generated SWs can be used in various applications. Among them, a considerable number concerns gaseous media and in particular air. An example of SW application is dry cleaning of surfaces from various kinds of particle contaminants [6]. In that case, a fs laser is first focused in air at a certain distance away from a polluted wafer with its propagation axis being parallel to the wafer surface. The resulting SW interaction with the contaminant particles results in their removal with an efficiency strongly dependent on the gap distance between the focal spot and the wafer surface. Another example is supersonic flow control where a fs laser-generated plasma and resulting SW modify the air flow resulting in drag reduction [7,8]. Additionally in the case of laser machining of materials, it has been shown that fs laser-generated SWs in air may have an impact on the quality of processing [9]. Finally, a unique feature of fs lasers is that thermodynamic effects take place after the energy deposition ends, in contrast with longer pulses. Therefore, these fs laser-induced SWs could potentially be used to simulate the effect of local explosions and the resulting blast waves on their surrounding area, at the microscale level.

While the use of fs-laser-generated SWs in air has been demonstrated, the SW pressure is a poorly known parameter. Naturally, knowledge of this parameter along with the SW propagation geometry is crucial in modelling and thus efficient control of the above-mentioned processes.

Surprisingly and to the best of our knowledge, we found a single study treating this subject, which shows the capacity of the created shockwave to strongly influence fs pulse propagation in double-pulse GHz experiments [10]. In contrast with ns pulses that were extensively studied over the past few decades [11–17], no estimation about the shockwave pressure and propagation characteristics in gas have been presented so far. Investigation of fs-laser-generated SWs in air may provide insight into the more general laser-matter interaction topic. Especially in the case of solids, a plethora of applications would be concerned as fs laser-generated SWs are used for laser shock peening [18,19] or polymorphic transformations [20,21]. Measurements and knowledge of their characteristics are also crucial for avoiding detrimental effects during laser-machining as they might lead to mechanical defects such as formation of cracks around the processing region [22].

In this work, we thus investigate the generation and evolution of shockwaves in ambient air, induced by a single tightly-focused fs laser pulse. The incident power is set much below the critical power in air ($P_{cr} \cong 5.4$ GW at 1030 nm [23]), aiming to address the still unexplored excitation regime for SW generation and characterization far from filamentation-driven regime [24]. A home-built time-resolved, transmission microscope operated with visible light allows us to directly observe both the plasma formation in the first few hundreds of fs and the generation and propagation of the shockwave in space and time within a few ns range. Based on our observations of the shockwave propagation, we use the conservation laws and the equation of state of ideal gas to theoretically model the phenomenon. Following comparisons with experimental data, our simulations provide the SW pressure evolution in space as a function of time as well as the fraction of the incident laser pulse energy that is absorbed in air and is used in the generation of the SW.

2. Methodology

2.1. Pump-and-probe transmission microscope

We have developed a pump-and-probe transmission microscopy technique which experimental scheme can be seen in Fig. 1. The fs laser source is a diode-pumped linearly-polarized Yb-doped fiber laser (Satsuma, Amplitude Systèmes) with a fundamental wavelength λ of 1030 nm, 360-fs pulse duration (measured at full width half maximum), a maximum output pulse energy of 20 µJ and a repetition rate up to 250 kHz. The laser energy is highly stable with no long-term drift and
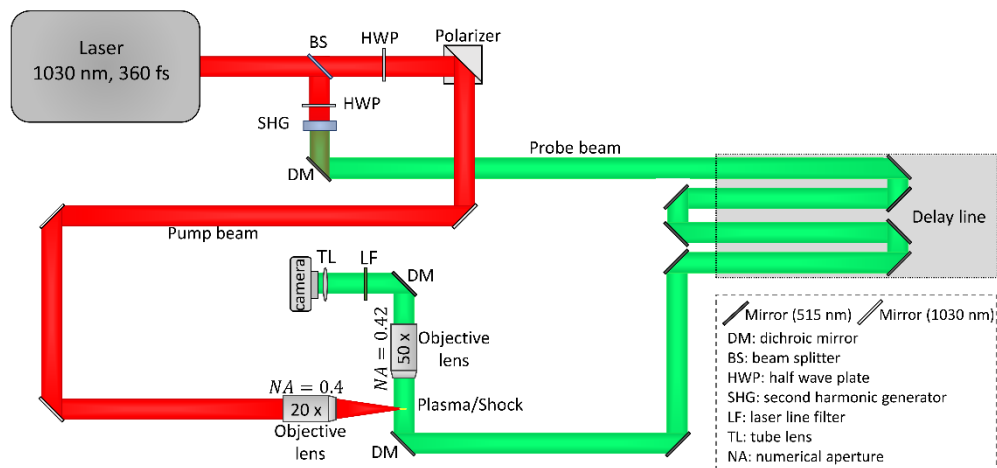

Fig. 1. Schematic illustration of the pump-probe experimental setup.

a pulse-to-pulse root mean square (RMS) stability less than 1.1%, measured at 250 kHz over 16 hours. Even if the pump-and-probe measurements are carried out using single laser shots, this is important for ensuring good precision and robustness of the experiments when scanning a large range of different time delays from femtosecond to nanosecond scale.

As shown in Fig. 1, the fs laser beam is initially divided into two parts with the help of a beam splitter (20% reflection, 80% transmission). The most energetic part of the beam (pump beam), that induces the air breakdown, passes through an energy attenuation system composed of a half-wave plate and a polarizer. The laser is focused in air with the help of a microscope objective lens (20x Mitutoyo Plan Apo NIR infinity corrected) with a numerical aperture (NA) of 0.4 and the entrance pupil completely filled. In these conditions, the focused spot diameter of the gaussian laser beam is calculated to be $2w_0 = \frac{0.82 \times \lambda}{NA} = 2.1$ μm, at $1/e^2$ of the maximum intensity distribution of an Airy disk. Thus, the incident laser intensities I of the pump pulse on the target (air) in the experiment, range from about 2.7 up to 4.9×10^{14} W/cm^2 (calculated as $I = \frac{E_p}{\pi w_0^2 \tau}$, where E_p is the pulse energy and τ the pulse duration). The less energetic beam part (probe beam) is converted to its second harmonic (at 515 nm) with the help of a type I second harmonic generation BBO crystal. It is subsequently used for the illumination of the pump-irradiated area in a perpendicular configuration providing femtosecond temporal resolution (supposed to be close to the probe pulse duration) and micrometric spatial resolution (0.6 μm according to the Abbe diffraction limit). The delay of the probe beam with respect to the pump can be adjusted by changing the optical path of the probe with a delay line, which is composed of a set of moving mirrors, within a range of about 5.5 ns. The illuminated area is then imaged with the help of an objective lens (50x Mitutoyo Plan Apo NIR infinity corrected) with 0.42 NA, and a CMOS camera (CS165MU Zelux, 3.45 μm square pixel size). Moreover, a dichroic mirror combined with a laser line filter at 515 nm before the camera is used to filter the detected probe beam from any parasitic light coming from plasma emission, scattering of the pump beam or even from the illumination of the room.

In order to improve the signal-to-noise ratio and thus acquire precise information about the change in transmission of the probe beam due to the effect of the pump beam, the probe images are divided by a reference image, which is obtained exactly in the same operating conditions but with the pump beam blocked. Using this approach, we observe the phenomenon from the laser-induced plasma formation in the first hundreds of fs up to about 5.5 ns after laser irradiation (limited by the length of the delay line), where the evolution of the emitted shockwave can be observed. As it will be shown later, plasma observation allows precise initialization of the simulations. The zero-time delay (t = 0) is defined as the instant at which a light-absorbing plasma is formed following nonlinear absorption of the pump pulse. More precisely, this instant corresponds to a drop in the probe transmission images.

2.2. Modelling

The commercial software Radioss from Altair Engineering Inc. is used to simulate SW propagation in air induced by the femtosecond laser energy deposition. It is an explicit finite element solver based on solid and fluid dynamics. The equation of state of the interaction medium (air) is described by the perfect gas law. The evolution of the pressure P is provided by the Law6 software modulus [25] which is expressed in its simplified form (Eq. (1)) as a function of the internal energy (per unit reference volume) ε of the system:

$$P = (\gamma - 1) \times \frac{\rho}{\rho_0} \varepsilon \tag{1}$$

In eq. (1), γ indicates the specific heat capacity ratio, taken equal to 1.4 considering air as a diatomic gas, ρ is the density of air and ρ_0, its initial unperturbed value at atmospheric pressure equal to $\rho_0 = 1.204 \times 10^{-3}$ g/cm^3.

Numerical 2D axisymmetric around (optical) z-axis simulations are further performed following the arbitrary Lagrangian-Eulerian approach. As schemed in Fig. 2, three spatial domains are defined. The first domain (in blue) corresponds to the initial volume in which the laser energy is swiftly deposited in air, further leading to the shockwave generation. This volume corresponds to the size of the experimentally observed laser-induced plasma (Fig. 3 b)). It is assumed ellipsoidal with the parameters "a" and "b" defining its two semiaxes. Note that these quantities vary insignificantly with respect to the laser excitation energy range (from 3 μJ to 5.5 μJ) considered in this work and so they will be kept constant in the modelling, set to 5 μm and 0.75 μm respectively. It is noteworthy to mention that the initial transverse size b of the laser energy deposition volume is below the diffraction-limited laser spot (approximately 1 μm at $1/e^2$) because of the predominance of multiphoton absorption in air at atmospheric pressure.
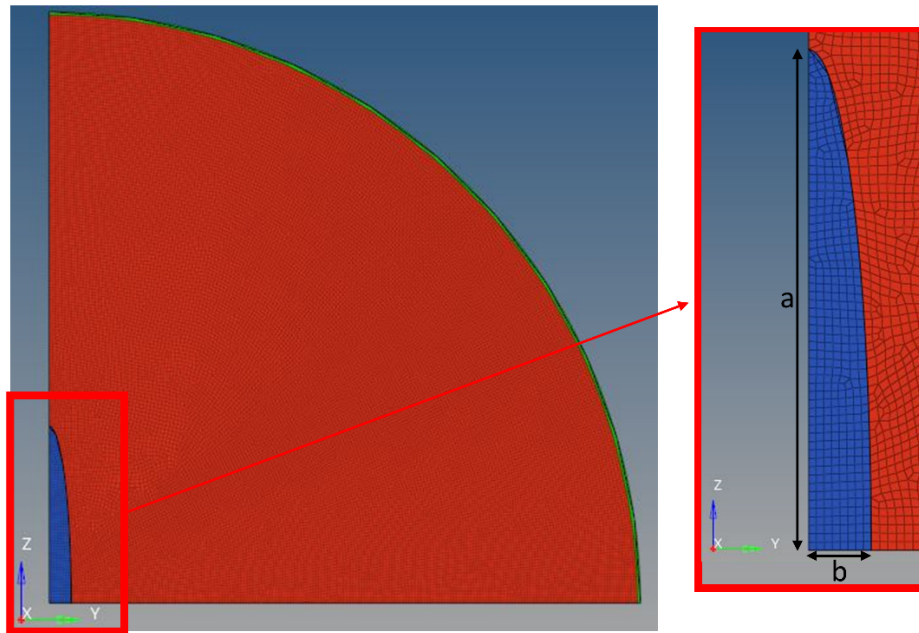

Fig. 2. Radioss 2D axisymmetric (around z-axis) numerical simulated configuration. The optical (laser) axis is along the z-axis. The labels "a" and "b" are the two semiaxes of the ellipsoid in which the energy deposition process takes place (in blue). The red area represents the domain where the shockwave propagates in air at room conditions. Silent bound conditions are shown in green to avoid reflection of waves.

The initial internal energy, which is necessary to define ε in this domain, is considered homogenously distributed in the ellipsoidal volume. It corresponds to the part of the laser absorbed energy dissipated to create the shockwave (E_{SW}). E_{SW} is numerically adjusted to best reproduce the experimental measurements of the shock wave propagation distance versus time (shown in Fig. 4). In support for that, we have performed a series of pump transmission measurements (shown in Fig.S1 in Supplement 1). We estimated that the percentage of incident laser energy that is conveyed to the shockwave channel is comparable with the percentage of the incident laser energy that is absorbed in air. For example in the case of 5.5 μJ incident laser energy, we found that air absorbs about 1.5% of it, while the adjusted E_{SW} value corresponds to approximately 1.3%. Note that, in practice, the SW is physically emitted at the periphery of the energy deposition volume (limit of the blue region). However, for sake of simplicity and without any consequences on the results shown hereafter, we suppose that it is emitted at the center of the

blue region. The second domain (in red) describes the area where the SW propagates, in which initial conditions are set to ambient room conditions (1 atm, 23°C). Finally, the third domain corresponding to the green layer is a silent bound (simulation condition to avoid wave reflection at the end of the studied domain).

3. Results and discussion

Applying the aforementioned pump-and-probe transmission microscopy technique, we measure the evolution of the shockwave propagation distance for four different incident pump pulse energies E_p, ranging from 3 µJ up to 5.5 µJ. We noticed that air breakdown occurs at about 1 µJ, corresponding to an intensity of 8×10^{13} W/cm². In the transmission images, the propagation distance of the shockwave front is defined with respect to its emission coordinates used in the modelling (corresponding to the center of the energy deposition volume). This propagation distance corresponds to the size of a fitted ellipse in the compressed area with α and β the major and minor semiaxis respectively. Figure 3 shows transmission images for a pump pulse of incident energy $E_p = 5$ µJ. Initially, at negative delays, at which the probe pulse arrives before the pump pulse, we cannot observe any feature in the transmission images (Fig. 3 a)). As delay increases in the first few hundreds of fs, we can observe the laser-induced plasma formation in air, as a narrow dark region with ellipsoidal shape (Fig. 3 b)). Long after the pump pulse ends, a supersonic expansion occurs and the shockwave can be clearly distinguished towards 100 ps
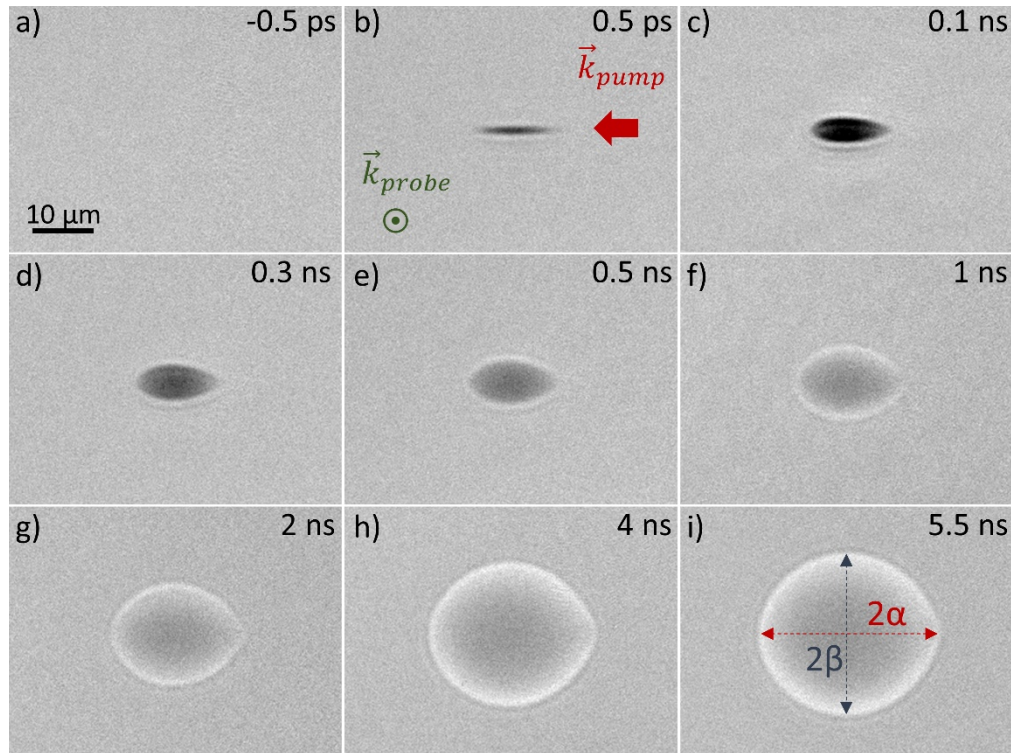

Fig. 3. Time-resolved pump-probe transmission images in air for 5-µJ incident pump pulse energy, with varying probe delays from a) 0.5 ps before pump irradiation, to b) plasma observation after pump pulse ends, and c) to i) observation of the ellipsoidal shockwave evolution within a few ns, with 2α and 2β in i) being the major and minor axes of the fitted ellipse.

yielding a thin overdense zone at the periphery of the plasma (Fig. 3 c)). Its evolution is observed within the next few ns (Fig. 3 d) to i)) and its propagation distance (α and β) is measured. The fitted ellipse has its long axis 2α along the direction of the optical axis and its short axis 2β along the axis perpendicular to the optical axis (as shown in Fig. 3 i)).

From the transmission images (Fig. 3), we also notice that the expansion of the shockwave is anisotropic for the two axes, as the ratio of 2α to 2β is not constant for all delays. This denotes that for our focusing conditions the shockwave does not exhibit the same behavior in the two axes, at least during the first few ns. We attribute it to our laser focusing conditions, which result in the deposition of the laser energy into a volume of ellipsoidal shape. Thus, the generated shockwave, which is emitted from the surface of this ellipsoid, commences its propagation with different initial velocities in the two directions (α and β) following the difference in deposited energy density along and transversely to the laser optical propagation. As the shockwave propagates in air, its pressure drops due to interaction of the compression wave with the medium and associated rarefaction wave and also the geometrical effect of the wave surface expansion. The velocity of the wave drops in a non-linear way towards the sound velocity. As a consequence, this anisotropy is observed during the supersonic expansion of the shockwave, and we expect it to last until the sonic limit is reached.

Using the model described in section 2.2, the evolution of the shockwave propagation distance is estimated in Fig. 4 as a comparison between the experimental measurements (colored symbols) and the corresponding simulated data from our model (colored lines). The simulated SW positions correspond to the position of the pressure maximum at a given time. This is done for the α and β semiaxes of the shockwave and for all four used incident energy E_p and their corresponding initial energy loadings (E_{SW}) used in the model. The error bars in the graph correspond to the spatial uncertainty related to the determination of the semiaxes of the fitted ellipse. From these graphs it is evident that the simulated curves match well the experimentally measured data for all four cases. As expected, the increase of E_p leads to the generation of shockwaves with higher energy loading E_{SW} and faster expansion. This increase in E_{SW} varies however in a nonlinear way with E_p from 0.15% for E_p equal to 3 μJ up to about 1.3% of E_p for the case of 5.5 μJ.

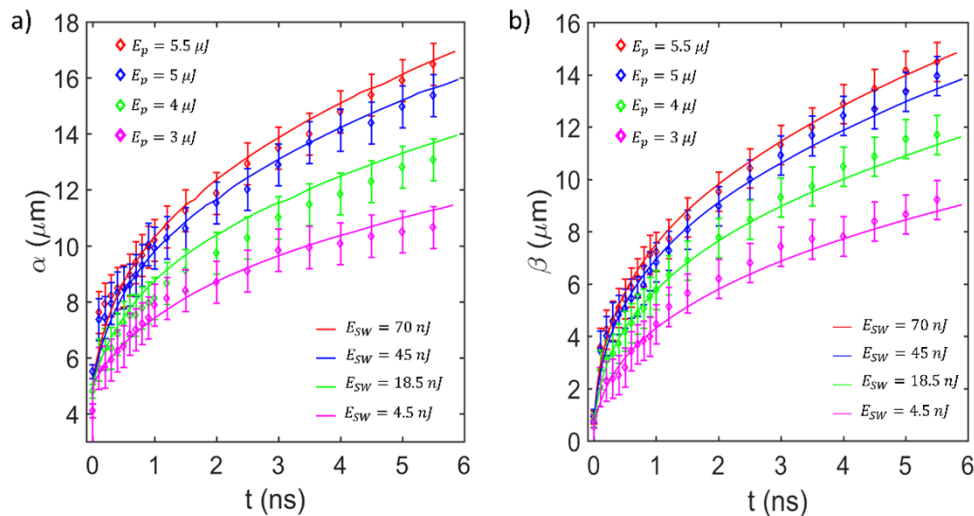**Fig. 4.** Evolution of the shockwave propagation distance based on our experimental measurements (symbols) and the model (lines) along the a) α semiaxis and b) β semiaxis of the ellipsoid, for 4 different incident pump pulse energies (E_p) and their corresponding shockwave initial energy loadings (E_{SW}) according to the model.

This indicates that the percentage of E_p that converts into mechanical energy in the form of a shockwave increases with E_p, resulting from higher degree of ionization of air particles at higher incident energy density. It is noticeable that the same increasing trend is observed from the pump absorption measurements in Fig. S2 of Supplement 1).

The very good agreement observed between experiments and simulations for the shockwave evolution over the whole range of our temporal observations justifies our initial consideration of air medium behaving as an ideal gas even for the highest energy deposition conditions. As a consequence, we can further apply the model to calculate the evolution of the SW pressure. The pressure evolution, derived from the model for all simulated cases of Fig. 4, is presented in Fig. 5 a). From this graph, it is noticeable that the initial pressure loading is in the range of GPa and within a few ns, the pressure drops about three orders of magnitude into the MPa range. As also observed previously, the pressure is not equal in the two directions along and perpendicular to the optical axis (α and β respectively). In all cases the pressure along β direction is higher than along α one. Recently, it was shown that laser-generated SWs in air can be used for mass/charge delivery into the optical path of a laser pulse resulting in increased THz emission efficiency [26]. The authors have achieved this by using double fs-laser pulses of 8-µm focal spots separated by 11 µm corresponding to a relative separation (separation distance over the focal spot diameter) of 1.375 times the laser spot. Interestingly, within the framework of our studies we have measured a maximum density increase of ~3 times the initial air density, 3 µm away from the center of the laser spot along Y axis (corresponding to the same relative separation as in [26]) for the maximum energy used.
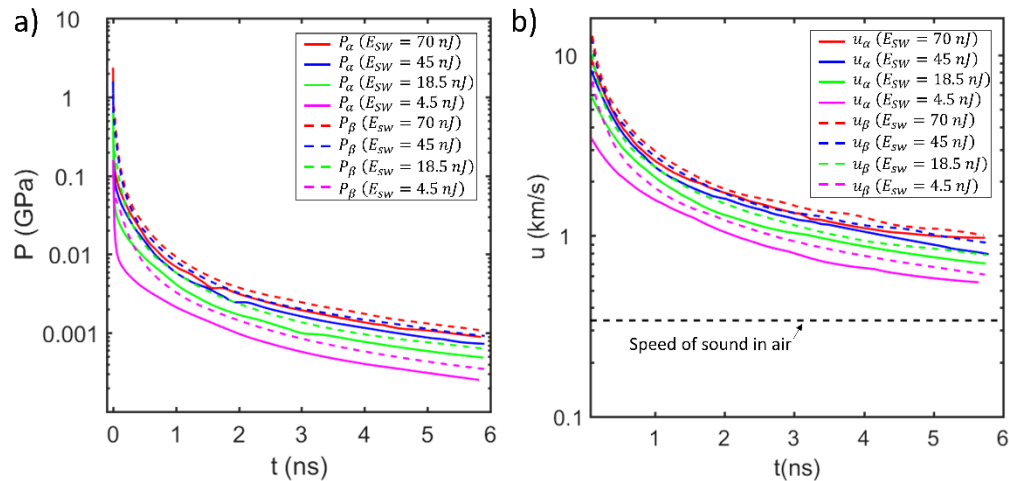

Fig. 5. Time evolution of the a) pressure and b) velocity of the shockwaves according to the model, for the two directions α (solid lines) and β (dashed lines) and for the four different initial energy loadings E_{SW} (different colors).

It is worthwhile to mention that the pressures reached are comparable with the ns laser-induced shockwave pressures needed for the cleaning of surfaces. For example, in the study of Kim et al. [27], a silicon surface is cleaned from alumina particles using a 1.7 MPa shockwave, and in the study of Kumar et al. [28], a steel substrate contaminated with uranium oxide particles is cleaned with the help of a 5 MPa shockwave. By reaching such shockwave amplitude with small incident energy (in comparison to the nanosecond case), femtosecond lasers provide inherent advantages for efficient small-scale damage-free cleaning as demonstrated in the works of Park et al. [6].

The evolution of the shockwave velocity according to the model can be seen in Fig. 5 b) for both α and β directions. The speed of sound in air at 23°C room temperature (0.33 km/s) is also

shown for comparison. Like pressure, velocity reaches higher values with the increase of initial energy loading and exhibits the same asymmetry for the two directions α and β, the expansion being faster along β direction. The initial velocity of the shockwave ranges between 3.5 and 13 km/s depending on the initial energy loading. Although it quickly drops close to 1 km/s within a few ns, it still remains in the supersonic regime throughout our observations. This indicates that the shockwave degenerates into an acoustic wave in a much later time delay. This may be of importance in perspective of laser material processing in air with multiple pulses [9] and/or at extremely high pulse repetition rate as now reached by commercial femtosecond laser sources [29].

4. Conclusions

We have experimentally observed the formation and evolution of fs laser-induced shockwaves with the help of a time-resolved transmission microscope, from the laser energy deposition up to 5.5 ns after. The laser energy deposition takes place within the first few hundreds of fs and the shockwave can be clearly measured at about 100 ps after laser irradiation. The shape of the generated shockwaves is ellipsoidal with the expansion being anisotropic for the two axes. This evolution is in very good agreement with our simple modelling approach, based on the conservation laws and the equation of state of ideal gas. According to our findings, in our focusing conditions (with NA ~ 0.4), most of the absorbed laser energy is converted into mechanical energy in the form of a shockwave with an initial pressure loading in the range of a few GPa and an initial velocity in the range of a few km/s. The pressure quickly drops in the MPa range within a few ns, but the shockwaves remain in the supersonic regime throughout the 5.5 ns range after femtosecond pulse energy deposition.

Disclosures. The authors declare no conflicts of interest.

Data availability. Data underlying the results presented in this paper are not publicly available at this time but may be obtained from the authors upon reasonable request.

Supplemental document. See Supplement 1 for supporting content.

References

1. K. Sugioka and Y. Cheng, "Ultrafast lasers-reliable tools for advanced materials processing," Light: Sci. Appl. **3**(4), e149 (2014).
2. K. C. Phillips, H. H. Gandhi, E. Mazur, and S. K. Sundaram, "Ultrafast laser processing of materials: a review," Adv. Opt. Photonics **7**(4), 684–712 (2015).
3. E. G. Gamaly and A. V. Rode, "Transient optical properties of dielectrics and semiconductors excited by an ultrashort laser pulse," J. Opt. Soc. Am. B **31**(11), C36–C43 (2014).
4. D. Tan, K. N. Sharafudeen, Y. Yue, and J. Qiu, "Femtosecond laser induced phenomena in transparent solid materials: Fundamentals and applications," Prog. Mater. Sci. **76**, 154–228 (2016).
5. K. Sugioka and Y. Cheng, *Ultrafast Laser Processing: From Micro- to Nanoscale* (CRC Press, 2013).
6. J. K. Park, J. W. Yoon, and S. H. Cho, "Removal of nanoparticles from a silicon wafer using plasma shockwaves excited with a femtosecond laser," Appl. Surf. Sci. **258**(17), 6379–6383 (2012).
7. C. M. Limbach, "Characterization of Nanosecond, Femtosecond and Dual Pulse Laser Energy Deposition in Air for Flow Control and Diagnostic Applications," Doctoral dissertation, Princeton University (2015).
8. P. Q. Elias, N. Severac, J. M. Luyssen, Y. B. André, I. Doudet, B. Wattellier, J. P. Tobeli, S. Albert, B. Mahieu, R. Bur, A. Mysyrowicz, and A. Houard, "Improving supersonic flights with femtosecond laser filamentation," Sci. Adv. **4**(11), eaau5239 (2018).
9. Q. Wang, L. Jiang, J. Sun, C. Pan, W. Han, G. Wang, F. Wang, K. Zhang, M. Li, and Y. Lu, "Structure-mediated excitation of air plasma and silicon plasma expansion in femtosecond laser pulses ablation," Research **2018**, 1–11 (2018).
10. N. Zhang, Z. Wu, K. Xu, and X. Zhu, "Characteristics of micro air plasma produced by double femtosecond laser pulses," Opt. Express **20**(3), 2528–2538 (2012).

11. A. M. Azzeer, A. S. Al-Dwayyan, M. S. Al-Salhi, A. M. Kamal, and M. A. Harith, "Optical probing of laser-induced shock waves in air," Appl. Phys. B Lasers Opt. **63**(3), 307–310 (1996).

12. H. Sobral, M. Villagrán-Muniz, R. Navarro-González, and A. C. Raga, "Temporal evolution of the shock wave and hot core air in laser induced plasma," Appl. Phys. Lett. **77**(20), 3158–3160 (2000).

13. M. Villagrán-Muniz, H. Sobral, and E. Camps, "Shadowgraphy and interferometry using a CW laser and a CCD of a laser-induced plasma in atmospheric air," IEEE Trans. Plasma Sci. **29**(4), 613–616 (2001).

14. M. Villagrán-Muniz, H. Sobral, and R. Navarro-González, "Shock and thermal wave study of laser-induced plasmas in air by the probe beam deflection technique," Meas. Sci. Technol. **14**(5), 614–618 (2003).

15. P. Gregorčič, J. Diaci, and J. Možina, "Two-dimensional measurements of laser-induced breakdown in air by high-speed two-frame shadowgraphy," Appl. Phys. A **112**(1), 49–55 (2013).

16. C. Song, X. Gao, and J. Wang, "Study on the collinear delay double pulse laser induced air plasma expansion by optical interference," Optik **127**(15), 6081–6086 (2016).

17. A. P. Singh, U. P. Padhi, and R. Joarder, "Propagation of Relativistic Shock Wave Induced by Laser Spark in Quiescent Air," in *Proceedings of the 7th International and 45th National Conference on Fluid Mechanics and Fluid Power (FMFP)* (2019), (163), pp. 1–4.

18. C. Lu, L. Ge, B. Zhu, Y. Li, X. Chen, X. Zeng, and Y. Chen, "Effective femtosecond laser shock peening on a Mg–3Gd alloy at low pulse energy 430 µJ of 1 kHz," J. Magnes. Alloy. **7**(3), 529–535 (2019).

19. Y. Sagisaka, M. Kamiya, M. Matsuda, and Y. Ohta, "Thin-sheet-metal bending by laser peen forming with femtosecond laser," J. Mater. Process. Technol. **210**(15), 2304–2309 (2010).

20. A. Vailionis, E. G. Gamaly, V. Mizeikis, W. Yang, A. V. Rode, and S. Juodkazis, "Evidence of superdense aluminium synthesized by ultrafast microexplosion," Nat. Commun. **2**(1), 445 (2011).

21. L. Rapp, B. Haberl, C. J. Pickard, J. E. Bradby, E. G. Gamaly, J. S. Williams, and A. V. Rode, "Experimental evidence of new tetragonal polymorphs of silicon formed through ultrafast laser-induced confined microexplosion," Nat. Commun. **6**(1), 7555 (2015).

22. Y. Ito, R. Shinomoto, A. Otsu, K. Nagato, and N. Sugita, "Dynamics of pressure waves during femtosecond laser processing of glass," Opt. Express **27**(20), 29158–29167 (2019).

23. S. P. O'Connor, C. B. Marble, D. T. Nodurft, G. D. Noojin, A. R. Boretsky, A. W. Wharmby, M. O. Scully, and V. V. Yakovlev, "Filamentation in Atmospheric Air with Tunable 1100–2400 nm Near-Infrared Femtosecond Laser Source," Sci. Rep. **9**(1), 12049 (2019).

24. A. Couairon and A. Mysyrowicz, "Femtosecond filamentation in transparent media," Phys. Rep. **441**(2-4), 47–189 (2007).

25. Altair Engineering, "Radioss theory manual," https://altairhyperworks.com/hwhelp/Altair/hw14.0/help/hwsolvers/theory_mat_laws.pdf.

26. H. Huang, S. Juodkazis, E. G. Gamaly, T. Nagashima, T. Yonezawa, and K. Hatanaka, "Spatio-temporal control of THz emission," Commun. Phys. **5**(1), 134 (2022).

27. D. Kim, B. Oh, D. Jang, J. W. Lee, and J. M. Lee, "Experimental and theoretical analysis of the laser shock cleaning process for nanoscale particle removal," Appl. Surf. Sci. **253**(19), 8322–8327 (2007).

28. A. Kumar, M. Prasad, R. B. Bhatt, P. G. Behere, and D. J. Biswas, "A comparative study on laser induced shock cleaning of radioactive contaminants in air and water," Opt. Laser Technol. **100**, 133–138 (2018).

29. E. Audouard, G. Bonamis, C. Honninger, and E. Mottay, "GHz femtosecond processing with agile high-power laser High power and flexible fs lasers in GHz burst mode open new horizons for femtosecond laser processing," Adv. Opt. Technol. **10**(4-5), 263–275 (2021).